Simulations of shock wave/turbulent boundary layer interaction with upstream micro vortex generators

Arnaud Grébert*, Julien Bodart, Stéphane Jamme, Laurent Joly

Department of Aerodynamics and Propulsion (DAEP), ISAE-SUPAERO, University of Toulouse, 10 Avenue Edouard Belin, Toulouse, 31055, France

A B S T R A C T

The streamwise breathing motion of the separation bubble, triggered by the shock wave/boundary layer interaction (SBLI) at large Mach number, is known to yield wall pressure and aerodynamic load fluctuations. Following the experiments by Wang et al. (2012), we aim to evaluate and understand how the introduction of microramp vortex generators (mVGs) upstream the interaction may reduce the amplitude of these fluctuations. We first perform a reference large-eddy simulation (LES) of the canonical situation when the interaction occurs between the turbulent boundary layer (TBL) over a flat plate at Mach number $M = 2.7$ and Reynolds number $Re_\theta = 3600$ and an incident oblique shock wave produced on an opposite wall. A high-resolution simulation is then performed including a rake of microramps protruding by 0.47δ in the TBL. The long time integration of the simulations allows to capture 52 and 32 low-frequency oscillations for the natural case and controlled SBLI, respectively. In the natural case, we retrieve the pressure fluctuations associated with the reflected shock foot motions at low-frequency characterized by $St_L = 0.02 - 0.06$. The controlled case reveals a complex interaction between the otherwise two-dimensional separation bubble and the array of hairpin vortices shed at a much higher frequency $St_L = 2.4$ by the mVGs rake. The effect on the map of averaged wall shear stress and on the pressure load fluctuations in the interaction zone is described, with a 20% and 9% reduction of the mean separated area and pressure load fluctuations, respectively. Furthermore, the controlled SBLI exhibits a new oscillating motion of the reflected shock foot, varying in the spanwise direction with a characteristic low-frequency of $St_L = 0.1$ in the wake of the mVGs and $St_L = 0.05$ in between.

1. Introduction

Because it is ubiquitous in high Mach number internal and external flows of interest to aeronautical applications, the shock wave/turbulent boundary layer interaction (SBLI) has been the focus of many research efforts over the past decades (see the review by Clemens and Narayanaswamy, 2014). There are different flow arrangements in which the SBLI occurs, depending on the geometry and the position of the shock generator relative to the boundary layer. However, they all exhibit a large separation bubble triggered by the severe adverse pressure gradient across the shock. The massive separation gives rise to two different issues from the application standpoint. Whereas load losses at the inlet of a scramjet engine are concerned with the impact on the engine efficiency of the mean flow properties, the structural fatigue by buffet modes over transonic airfoils is due to the unsteadiness of the SBLI. We restrict ourselves to the simplest configuration that illustrates the second kind of preoccupations where an incident oblique shock wave impinges on a flat plate turbulent boundary layer (TBL).

In large upstream Mach number SBLI, the separation point and the reflected shock foot are well known to oscillate in streamwise direction at a frequency f much lower than the inverse of the characteristic travel time over the separation bubble length L_{sep}. The corresponding Strouhal number $St_L = fL_{sep}/U_\infty$ is thus small and lies in the range $0.02 - 0.06$. Though very slow, the streamwise motion of the reflected shock yields large amplitude variations of pressure signals measured at fixed positions on the wall that are alternatively located upstream and downstream the moving reflected shock foot.

No consensus about the origin of this low-frequency motion has emerged yet but two explanations are standing as good candidates and have largely benefited from recent refined simulations or upgraded experimental measurement techniques.

According to the PIV measurements carried out by Piponniau et al. (2009), the recirculating region would be drained at low frequencies in response to the KH instability of the shear layer developing along the separation line. On the other hand, Ganapathisubramani et al. (2009) report that unsteadiness is linked to

* Corresponding author.
E-mail address: arnaud.grebert@isae.fr (A. Grébert).

https://doi.org/10.1016/j.ijheatfluidflow.2018.05.001

the presence of long streamwise boundary-layer superstructures located in the lower part of the upstream boundary layer, which leads them to conclude that the low-frequency motion observed in SBLI corresponds to a selective amplification of large-scale disturbances in the incoming flow.

Besides, a great deal of effort has been directed to reduce the SBLI-induced impact on aerodynamic performances or load variations relying on classical passive control solutions, such as streamwise vortex generators, aiming at delaying or suppressing separation. Among these, vortex generators smaller than the TBL thickness, also called microramp vortex generators (mVGs), have drawn a particular attention because their induced drag remains low while they significantly enhance wall-normal momentum transfer (Lin, 2002).

In the context of SBLI Anderson et al. (2006) conducted a comprehensive evaluation by steady RANS simulations of a large number of mVGs designs to increase the recovery rate of the TBL downstream reattachment, *i.e.* to minimize the boundary layer transformed form factor H_{tr} downstream of the SBLI. Following the experimental study of Wang et al. (2012) we select the mVG rake geometry that was identified as optimal by Anderson in this respect. However, before addressing the impact of the mVGs rake on the SBLI, the flow structure downstream of the mVGs is of interest on its own (see Panaras and Lu, 2015). In Grébert et al. (2016) we confirmed that the mVG wake exhibits a highly periodic vortex shedding with counter-rotating vortex pairs forming hairpin vortices downstream.

The present large eddy simulations (LES) thus aim at clarifying the interaction between the unsteady mVGs wake and the separation bubble behind the reflected shock. We are able to compare the natural SBLI and the one impinged by the mVGs wake with respect to the frequency content of the wall-pressure fluctuations, to wall shear stress and pressure load fluctuations. We also advocate that these numerical simulations could ultimately give hints about the uncontrolled low-frequency motion mechanism.

2. Flow configuration

2.1. Large-eddy simulations set-up

This study follows our previous work and all details about the numerics and validation of the simulations can be found in Grébert et al. (2016, 2017). The present large eddy simulations were performed using the `CharLES`^{x} solver, see Bermejo-Moreno et al. (2014), which solves the spatially filtered compressible Navier–Stokes equations for conserved quantities using a finite volume formulation and a control-volume-based discretization on unstructured hexahedral meshes. An explicit third-order Runge–Kutta (RK3) scheme is used for time advancement. The solver relies on Vreman (2004) subgrid-scale (SGS) model to represent effect of unresolved small-scale fluid motions. It also features a solution-adaptive methodology which combines a non-dissipative centred numerical scheme and an essentially non-oscillatory (ENO) second-order shock-capturing scheme. The latter is applied in regions around shock waves, identified by a shock sensor sensitized (Eq. (1)) to local dilatation $\partial u_k/\partial x_k$, enstrophy $\omega_i\omega_j$, sound speed c and mesh cell size Δ (see Bermejo-Moreno et al., 2014 for more details about the numerics).

$$-\frac{\partial u_k}{\partial x_k} > \max\left(\sqrt{\omega_i\omega_j}, \frac{0.05c}{\Delta}\right) \tag{1}$$

The configuration selected in the present work follows Wang et al. (2012) experiments, as sketched in Fig. 2. It is characterized by a free stream Mach number of $M = 2.7$ and a Reynolds number $Re_\theta = 3600$ based on the turbulent boundary layer momentum thickness at the wall inviscid-impingement location of the incident shock x_{imp}. As in the experiments, a shock generator is introduced on the opposite wall with a flow deflection of $\phi = 10.5°$ yielding to an incident shock wave angle of $\beta = 33.3°$. The microramp vortex generator (mVG) geometry is

Table 1
Grid parameters for the LES with δ_0 the TBL thickness just upstream of the SBLI at $x_A^* = -1.5$.

Δx^+	$\Delta y^+_{\min}$	Δz^+	L_x/δ_0	L_y/δ_0	L_z/δ_0
[7.5–20]	1	[3–15]	40	12	6

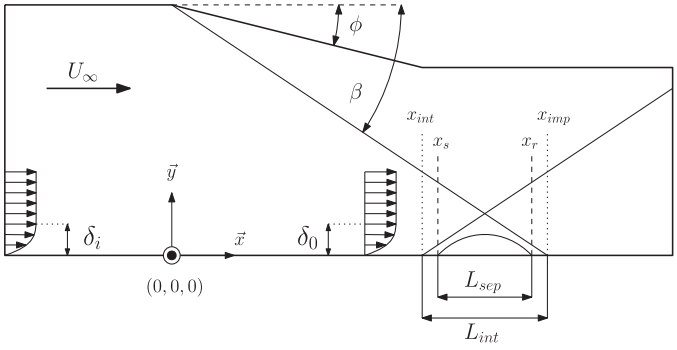

Fig. 1. Schematic of the SBLI configuration with reference parameters and length scales.

the same as in the experiments with a height of where δ_v is the TBL thickness immediately upstream of the mVG, a chord length $c = 7.2h$ and a wedge half-angle $A_p = 24°$. Two spanwise periods of the mVGs rake are introduced in the computational domain, located at $16\delta_v = 34h$ from the impingement shock incident point and at $23\delta_i$ from the inlet, δ_i being the TBL thickness at the inflow, to avoid spurious effect of the

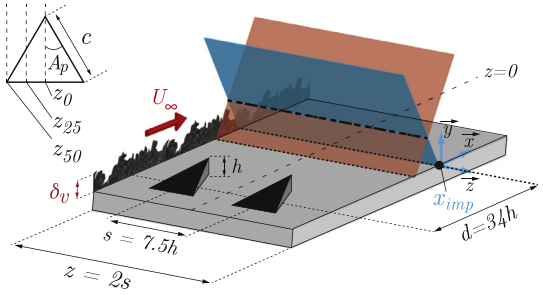

Fig. 2. Sketch and reference length scales of the configuration for the present LES with microramp vortex generators.

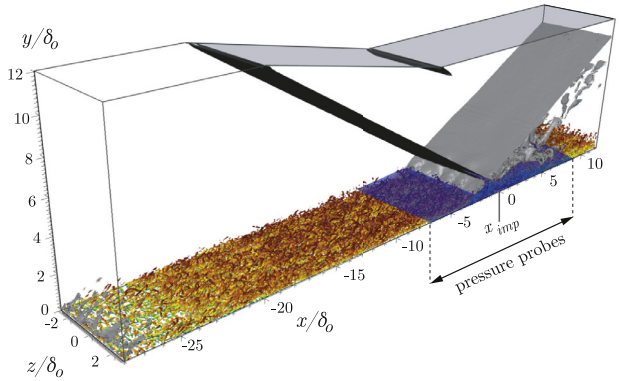

Fig. 3. Schematic view of the wall-pressure probes area (blue). (For interpretation of the references to colour in this figure legend, the reader is referred to the web version of this article.)

inflow condition. Grid parameters are given in Table 1 where the lowest values in the range of Δx^+ and Δz^+ corresponds to the mesh refinement on the edges of the mVGs.

The turbulent boundary layer is established using the digital filter inlet conditions proposed by Xie and Castro (2008) and modified by Touber and Sandham (2009). The parameters of the digital filter are chosen according to Touber and Sandham (2009) prescription. The flat plate and mVGs are modelled as adiabatic no-slip walls, whereas symmetry conditions are used for the shock generator and the downstream top part of the computational domain. Periodicity is enforced for the lateral boundaries of the domain, and the outflow boundary condition uses linear extrapolation of all flow variables.

Two LES have been carried out on the same aforementioned computational domain. The first configuration is the baseline SBLI without control and the second one features two mVGs to control the SBLI. The baseline and controlled configurations are referred to as *case A* and *case B*, respectively. Subscripts $_A$ or $_B$ denote quantity related to one of these two configurations.

2.2. Incoming turbulent boundary layer

Prior to addressing the SBLI, we assess the main properties of the incoming turbulent boundary layer. Using the baseline configuration, *i.e.* without mVGs, the spatial development of a supersonic TBL is considered downstream of the inflow obtained using the digital filter approach. The van-Driest-transformed mean velocity profile and the RMS of the Reynolds stresses are plotted in Figs. 4 and 5, respectively. They are compared to the DNS data of Pirozzoli and Bernardini (2013) and Schlatter and Örlü (2010) for an identical Reynolds number $Re_\tau = 499$, corresponding to $x_A^* = -3$ in our simulation (see Fig. 16 for reference). The Reynolds stresses are reported using the van-Driest multiplier, semi local scaling, $\xi = \sqrt{\langle\rho\rangle/\rho_w}$, where $\langle\bullet\rangle$ denotes the time averaging and the subscript $_w$ refers to quantities at the wall. It should be noted that the DNS of Pirozzoli and Bernardini (2013) has a slightly different Mach number of $M = 3$ and that the DNS of Schlatter and Örlü (2010) is performed for incompressible flow conditions. The velocity profile displayed in Fig. 4 is in good agreement with the logarithmic law of the wall and the DNS data, especially with the data from Pirozzoli and Bernardini (2013). The Reynolds normal stresses $\langle u_i' u_i' \rangle$ are in an overall good agreement with DNS data. However, the turbulent shear stress $\langle u'v' \rangle$ is slightly overestimated over the whole TBL.

For further validation, the streamwise evolution of the incompressible skin friction coefficient, obtained using the van-Driest II transformation (van Driest, 1951), is plotted in Fig. 6. The time-averaged skin-friction coefficient $\langle C_{f_i} \rangle$ is in very good agreement with the DNS results of Schlatter and Örlü (2010) and the LES results of Eitel-Amor et al. (2014).

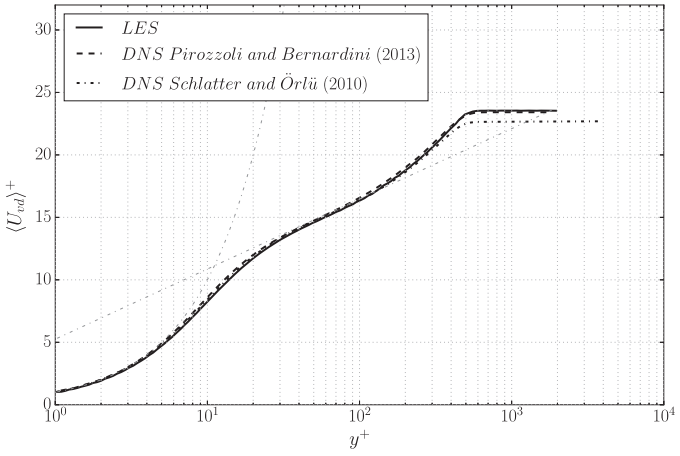

Fig. 4. van-Driest transformed mean-velocity profile compared to references at $Re_\tau = 499$.

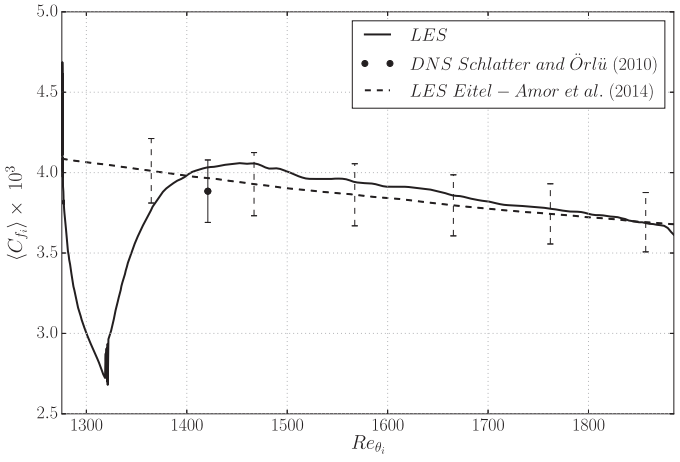

Fig. 6. Incompressible skin friction coefficient evolution. Error bars indicates ± 5% of value.

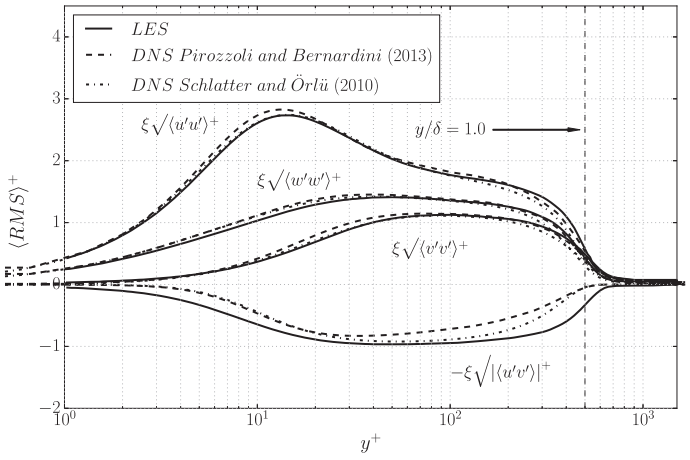

Fig. 5. RMS of Reynolds Stresses with density scaling $\xi = \sqrt{\langle\rho\rangle/\rho_w}$ at $Re_\tau = 499$.

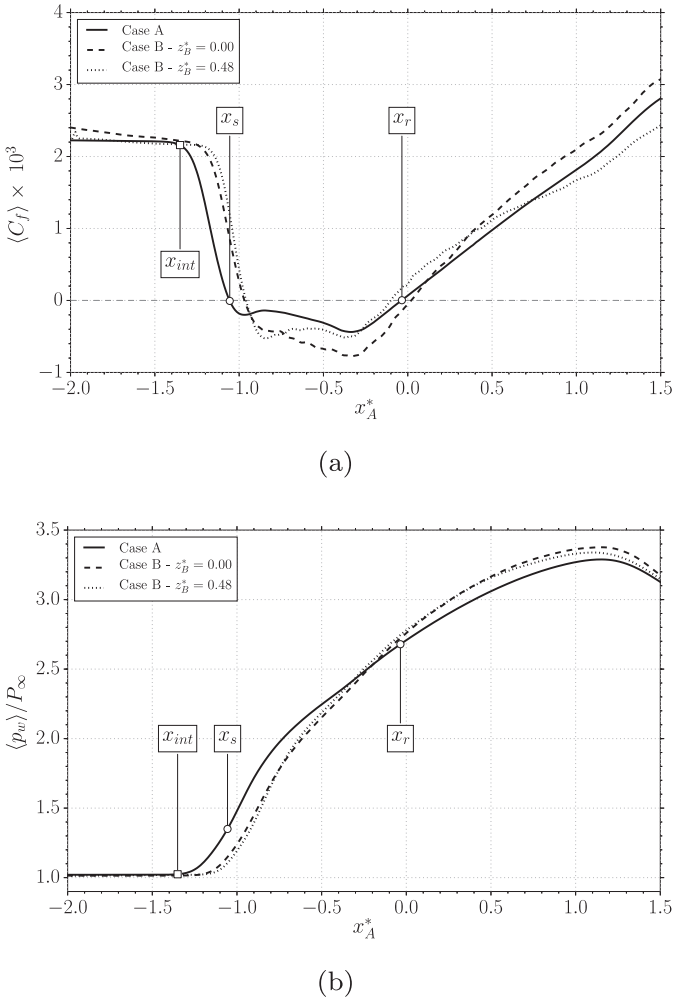

Fig. 7. (a) Skin-friction and (b) wall-pressure evolutions for cases A and B. Reported quantities are: time and spanwise averaged for case A (—); time and spanwise periodically averaged for case B (- - -) between the mVGs, and (.....) in the centreline of the mVGs. x_{int}, x_s and x_r indicate, for case A, the mean starting point of the interaction region, the mean separation and reattachment locations, respectively.

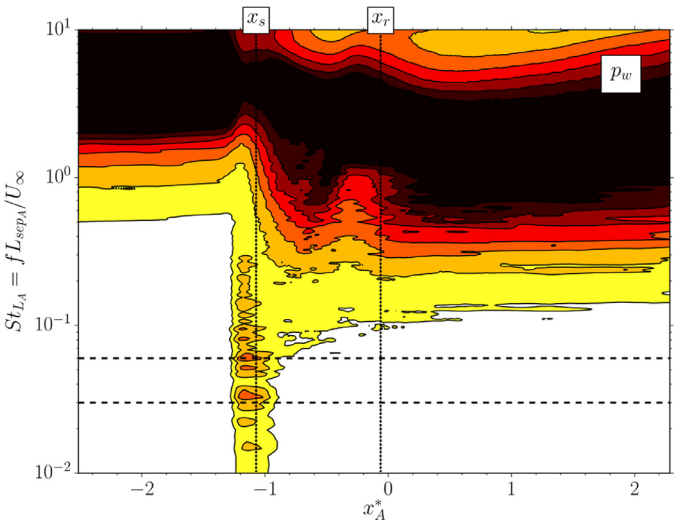

Fig. 8. Spanwise-averaged weighted spectra of wall-pressure, normalized by local $\int PSD(x, f)df$.

3. Results and discussion

3.1. Shock wave/turbulent boundary layer interaction

We now focus on the SBLI system without control (case A). In the region of the SBLI, the flow is decelerated due to the adverse pressure gradient imposed to the turbulent boundary layer. As a consequence, a separation bubble forms between the incident and reflected shocks where reverse flow conditions are associated with negative skin friction coefficient. Fig. 7 shows the streamwise evolutions, with $x_A^* = (x - x_{imp})/L_{sep_A}$ the reduced streamwise coordinates, of the skin friction coefficient C_f and wall-pressure p_w. The mean separation length L_{sep_A} is determined using the mean skin friction coefficient $\langle C_f \rangle$ (Fig. 7(a)) and results in our LES to $L_{sep_A} = 3.51\delta_0$, where δ_0 is the TBL thickness computed at $1.5L_{sep_A}$ upstream of x_{imp}, *i.e.* at $x_A^* = -1.5$. The mean interaction length L_{int} is computed between the inviscid impingement point of the incident shock wave x_{imp} and the mean starting point x_{int} of the interaction, see Fig. 1. This mean starting point is obtained using the evolution of the mean wall pressure by detecting an increase that exceeds 1% of the undisturbed TBL wall pressure value, Fig. 7(b). For the present LES, we find $L_{int} = 4.75\delta_0$, which is in good agreement with the values in the literature (Aubard et al., 2013; Touber and Sandham, 2009) but established at $M = 2.3$ instead of $M = 2.7$. No measurement of these length scales were performed by Wang et al. (2012).

The subsequent results will now focus on the analysis of the unsteadiness of the present SBLI by means of spectral analysis. We placed 31 600 probes at the wall (see Fig. 3) in the interaction region covering the complete span of the computational domain $z_A^* = [-0.8, 0.8]$ and covering the complete interaction region $x_A^* = [-2.8, 2.6]$. These probes are sampled at very high frequency ($St_{L_A} = 120$) in order to capture all the frequency content in the incoming TBL and the total integration time enables to capture 52 low-frequency oscillations with a minimum resolvable Strouhal number of $St_{L_A} = 5.8.\,10^{-4}$. The following wall-pressure spectra are obtained using Welch's algorithm with Hann window for a total number of 10 segments and a 50% overlap. This allows a total window length of $165L_{sep_A}/U_\infty$. Furthermore, a Konno–Omachi smoothing filter (Konno and Ohmachi, 1998) is applied to all spectra computed.

Fig. 8 shows the classical spanwise-averaged weighted power spectral density map with local scaling. The spectral analysis is carried out on the wall-pressure signal at each available spanwise station and then spanwise averaging is performed. Moreover, the spectra are normalized at each streamwise station by the local integral of the PSD. Horizontal dashed lines show $St_{L_A} = [0.03, 0.06]$ and vertical dotted lines indicate the location of the mean separation and reattachment locations.

A first remark is that no energetically significant content appears in the low or medium-frequency ranges appears in the upstream TBL, emphasizing the suitability of the digital filter approach used to generate the incoming TBL. Just upstream of the mean separation location, a significant broadband energetic content can be seen at low-frequencies $St_{L_A} = [0.02, 0.08]$, associated with the low-frequency motion of the reflected shock foot. This is in agreement with numerous numerical and experimental studies (Dupont et al., 2006; Touber and Sandham, 2009; Priebe and Martín, 2012; Grilli et al., 2012; Pasquariello et al., 2017). In the present LES, two peaks can be observed in this low-frequency range, $St_{L_A} = 0.033$ and $St_{L_A} = 0.06$, the latter being the most energetic one. Past the mean separation location the energetic scales are shifted toward higher frequencies, but they mostly remain below the ones in the undisturbed TBL. In the middle of the mean separation bubble, a significant energy content appears in the medium frequency range ($0.5 < St_{L_A} < 0.8$), which is classically related to the shear-layer vortices that form along the dividing streamline. Downstream of the interaction, past the mean reattachment location, the lowest energetic scales still lie in this medium frequency range. Due

to the thickening of the downstream TBL, characteristic turbulent scales exhibit lower frequencies compared to the upstream boundary layer.

As we have just seen, the main characteristics of the interaction region can be highlighted using the conventional representation of the wall-pressure spectra. However, in order to emphasize the two-dimensional dynamics of the SBLI we present in Fig. 9 the weighted spectra of spanwise-averaged wall-pressure fluctuations with various scalings, using the same methodology as in the aforementioned results. Contrary to the results in Fig. 8, wall-pressure signals are here spanwise-averaged first before performing the spectral analysis. The new weighted PSD map with local scaling is shown in Fig. 9(a). It should be noted that the energetic content in the incoming TBL is expected to be zero since spanwise average of the wall-pressure fluctuations is used. As it will be discussed further below, this is indeed the case in our results even it does not seem to be true when using local scaling of the finite lengths of the signals. Despite this weakness, this kind of representation allows to highlight more clearly the same broadband energetically significant content near the mean separation location as the one observed in Fig. 8, with very large peaks at $St_{L_A} = [0.015, 0.038, 0.051, 0.062]$. In the second

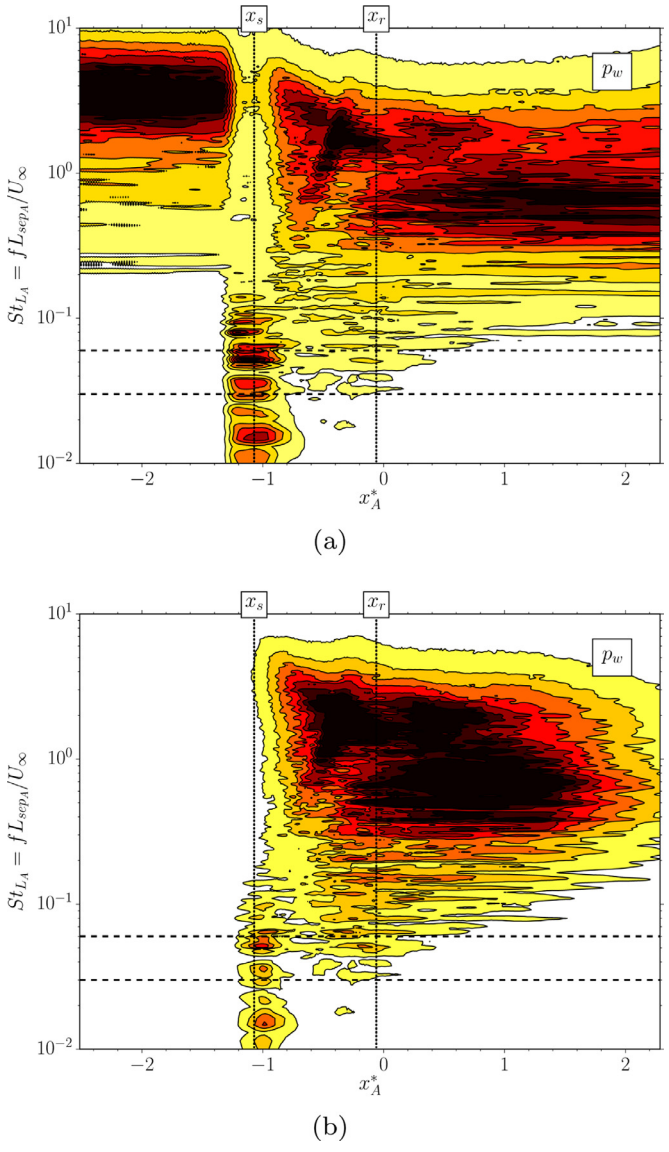

Fig. 9. Weighted PSD map of spanwise-averaged wall-pressure fluctuations normalized by (a) local $\int PSD(x, f)\mathrm{d}f$, (b) global maximum of $\int PSD(x, f)\mathrm{d}f$. Mean separation x_s and reattachment x_r locations are indicated by vertical dotted lines.

half of the separation bubble, a high energetic two-dimensional content can be observed at high frequencies ranging from $1.0 < St_{L_A} < 2.0$ with a small ridge centred on $St_{L_A} = 1.85$. In the downstream region, two convective ridges appear in the medium frequency range at $St_{L_A} = [0.5, 0.66]$. Therefore, the dominant two-dimensional dynamics of the SBLI can be decomposed in three parts: The low-frequency motion of the reflected shock foot ($St_{L_A} = [0.015, 0.038, 0.051]$), a high frequency ($St_{L_A} = 1.85$) activity in the second half of the separated area and a medium frequency content ($St_{L_A} = [0.5, 0.66]$) related to the shedding of vortices.

When global scaling with the streamwise maximum of $\int PSD(x, f)\mathrm{d}f$ is used, we can observe in Fig. 9(b) that the upstream TBL energy content vanishes as expected. A broadband low-frequency content still exists in this representation with peaks centred at $St_{L_A} = [0.015, 0.038, 0.051]$. Moreover, it can clearly be seen that the most energetic scales of the SBLI lie in the separated area and are convected downstream. The separation bubble generates highly energetic two-dimensional structures at high frequencies that shift rapidly downstream of the interaction to the medium frequency range.

To gain further insight into the SBLI dynamics we performed a modal analysis by means of dynamic mode decomposition (DMD). To this end, we used the Python `modred-2.0.1` library (Belson et al., 2014) which was successfully used on similar SBLI configurations by Priebe et al. (2016). The use of DMD enables to extract modes and frequencies significance (dominant modes) by projecting the large scale flow problem onto a set of approximate eigenmodes. This allows to decompose fluid flows with complex temporal dynamics into coherent structures in space corresponding to the same temporal frequency (Schmid, 2010). All details about the numerics and DMD methodology can be found in Belson et al. (2014), Tu et al. (2013) and Jovanović et al. (2014). In the present work, DMD analysis is carried out on three-dimensional snapshots of the pressure field with a domain limited to $x_A^* = [-3.8, 1.9]$, $y/\delta_0 = [0, 3.6]$ and covering the entire span of the computational domain. This allows to capture the complete SBLI system together with the upstream and downstream regions of the interaction. This 3D DMD analysis was performed on 1175 three-dimensional snapshots saved during the computation with a constant sampling frequency of $St_{L_A} = 7.2$ to describe the high frequency dynamics. The total integration time used for the DMD analysis enabled to capture 5 low-frequency oscillations with a minimum resolvable Strouhal number of $St_{L_A} = 6.\ 10^{-3}$. The inner product between two flow fields q_1 and q_2 is defined for the flow domain $\mathscr{D}$ as:

$$\langle q_1, q_2 \rangle = \iiint_{\mathscr{D}} p_1 p_2 \ \mathrm{d}x\, \mathrm{d}y\, \mathrm{d}z \tag{2}$$

For the present DMD on a sequential time series, the choice of the inner product has little effect in our analysis of a large dataset describing a stationary process, as mentioned by Priebe et al. (2016).

In Fig. 10 we show the DMD eigenvalues spectra of our three-dimensional pressure field database. Fig. 10(a) displays the spectrum of the modulus decay rate computed using $\rho_i = |\mu_i|$, where μ_i are the DMD eigenvalues. Associated frequencies are obtained with $f_i = \arg(\mu_i)/2\pi\Delta t$, where Δt is the sampling time interval. It should be noted that for the sake of clarity, only DMD modes with a decay rate $\rho_i \geq 0.995$ are represented, excluding rapidly decaying modes (89 modes excluded out of a total of 1174 modes). In order to identify the relevant DMD modes, we show in Fig. 10(b) the spectral coefficient of the DMD modes. These coefficients are obtained from a biorthogonal projection of the last snapshots onto the exact DMD modes. Therefore, modes with highest $||d||$ can be seen as those affecting the flow field over the entire temporal evolution. Note that we present in Fig. 10(b) the same selection of modes as in Fig. 10(a). Finally, the relevant modes for this study are highlighted in Fig. 10 by white bullets (○). In Fig. 10(c), we only focus on the modes with a decay rate larger than 1 or very close to unity ($\rho_i \geq 0.9999$), *i.e.* the growing or stable modes. These modes are the only ones considered in the following analysis.

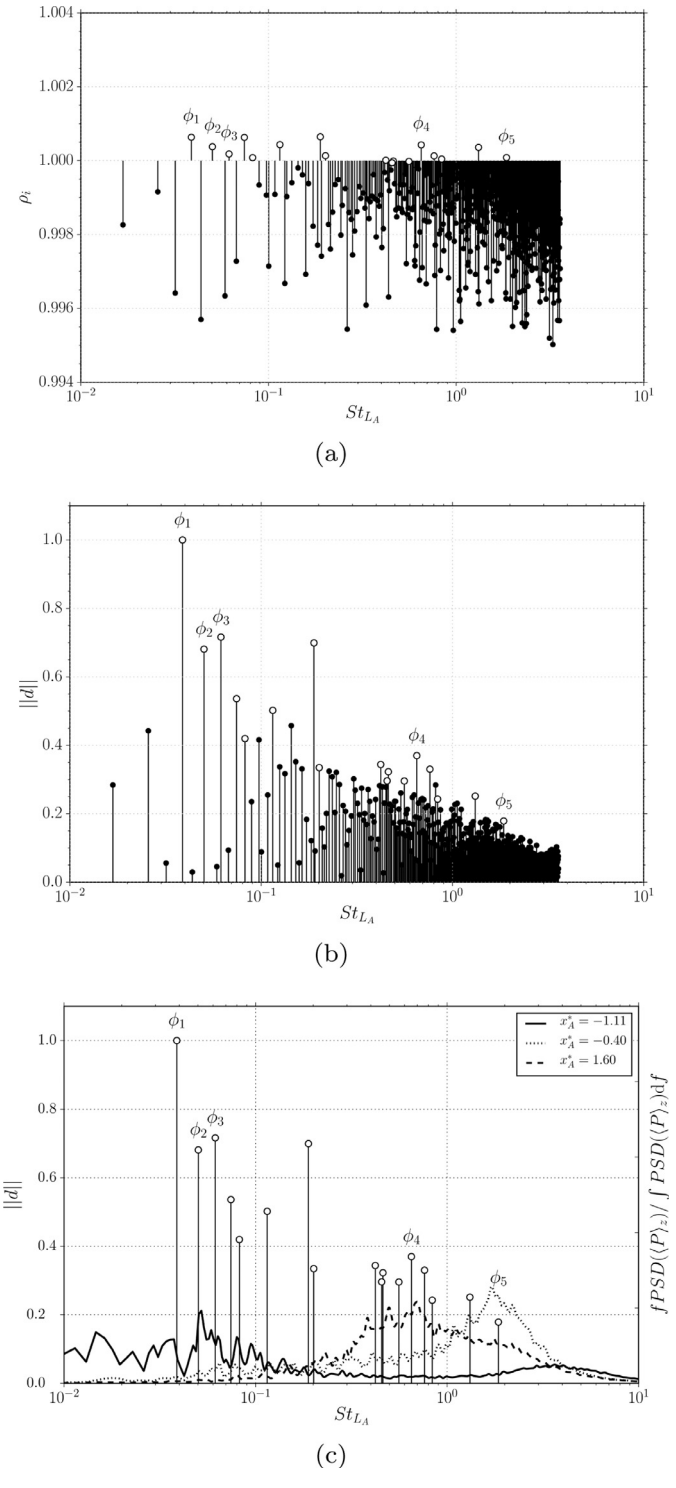

Fig. 10. DMD results for the three-dimensional pressure flow field, (○) indicate growing modes. (a) Modulus decay rate ρ_i of eigenvalues (DMD modes with $\rho_i < 0.995$ are not shown in this figure). (b) Spectrum of eigenvalues. (c) Spectrum of growing modes and weighted PSD of spanwise-averaged wall-pressure at selected locations $x_A^* = [-1.1, -0.4, 1.6]$. Refer to Fig. 9 for a physical interpretation of the streamwise locations.

In an attempt to associate the frequencies of the energy containing modes to the global flow phenomena, we superimposed to the spectrum of the selected modes, the weighted PSD of spanwise-averaged wall-pressure fluctuations at three key locations in the interaction region based on the density map in Fig. 9. These streamwise positions correspond to the reflected shock foot, second half of the separation bubble and region downstream of the SBLI. It can clearly be seen that almost all low-frequency DMD modes are well associated with the low-frequency motion of the reflected shock foot. Regarding the recirculating zone, the high-frequency DMD modes correlate very well with the peak of the wall-pressure spectrum at $x_A^* = -0.4$. Finally, the mid-frequency modes are clearly associated with the coherent structures convected downstream of the SBLI based on the PSD computed at $x_A^* = 1.6$.

In the following we analyze more thoroughly only a subset of modes among those highlighted in Fig. 10(c). These selected modes are denoted $\phi_{1..5}$, and their associated real part derived from the DMD algorithm are presented in Fig. 11. In order to provide additional insight on the isolated contribution of these selected modes on the overall flow behaviour, we also provide animations of the selected modes modulation on the mean-flow as supplementary materials online. Following Pasquariello et al. (2017), we reconstruct the pressure field modulation corresponding to the selected mode $\boldsymbol{\phi_i}$ according to: $p(\mathbf{x}, t) = \boldsymbol{\phi_m} + a_f \cdot \Re\{\boldsymbol{\phi_i} e^{i\omega_i t} + c.c.\}$, where $\boldsymbol{\phi_m}$ denotes the mean mode, $c.c.$ indicates the complex conjugate contribution and a_f is an amplification factor set to 10 in the present work. The growth rate is neglected since we only focus here on the oscillatory behaviour of the selected growing modes. The supplementary animations show iso-surface of the pressure gradient magnitude $|\nabla p|\delta_0/p_\infty = 2.5$ coloured by the pressure p.

Fig. 11(a) to (c) present the real value of the modes associated with low-frequency motion of the reflected shock foot. It can clearly be seen that the corresponding pressure fluctuations are located on the reflected shock and downstream compression waves. The corresponding modes animations available online show the iso-surface of the pressure gradient magnitude at 8 equally spaced phase angles. One can observe that the mode ϕ_1 at $St_{L_A} = 0.039$ exhibits mainly a translation motion of the reflected shock whereas the mode ϕ_2 at $St_{L_A} = 0.05$ shows mostly a spanwise oscillation of this shock wave. These modes correspond to the highly energetic two-dimensional frequencies highlighted in Fig. 9. It should be noted that the spanwise wavelength of mode ϕ_2 oscillations corresponds to the size of the computational domain in this direction. In order to investigate the physical significance of this phenomenon, a new computation has been performed with an increased span length from $L_z = 6\delta_0$ (for the reference case A) to $L_z = 10.5\delta_0$. The same DMD methodology has been applied and Fig. 11(f) shows the separation and reattachment lines of the DMD mode ϕ_2 ($St_{L_A} = 0.05$) for both domain sizes. These lines are identified, for each spanwise width L_z, using the wall-pressure iso-values $p_w/p_\infty = 1.3$ and $p_w/p_\infty = 2.7$, see Fig. 7(b). The extended domain still exhibits a spanwise modulation of the SBLI but with a wavelength equal to $L_z/2$, *i.e.* $5.25\delta_0$. This finding confirms the existence of a spanwise undulation motion of the reflected shock foot and separated area, the latter being consistent with the findings of Hildebrand et al. (2018) and Pasquariello et al. (2017) who reported a spanwise modulation of the separated area and specifically its reattachment line.

The last low-frequency mode ϕ_3 at $St_{L_A} = 0.062$ is a combination of these two motion types. Interestingly, and contrary to modes ϕ_1 and ϕ_2, this mode also features strong pressure field modulations in the separated area, in the vicinity of the separation line and in the recirculation bubble, as well as in the downstream part of the SBLI (in the TBL and reattachment compression waves). These pressure field modulations are clearly observable in the side-view animation corresponding to ϕ_3. This $St_{L_A} = 0.062$ frequency could thus be linked to the instabilities created in the separation bubble that are convected downstream of the SBLI region.

Regarding the medium frequency range mode ϕ_4 at $St_{L_A} = 0.652$, Fig. 11(d), we observe modulations of the pressure field located in the SBLI and downstream region close to the interaction. The shape of these modulations share some similarities with the low-frequency range modes with high levels of pressure fluctuations along the reflected shock foot. Animation of this mode shows activity in the separation bubble together with spanwise highly coherent structures modulating the wall-pressure downstream of the SBLI. The modal shapes of this

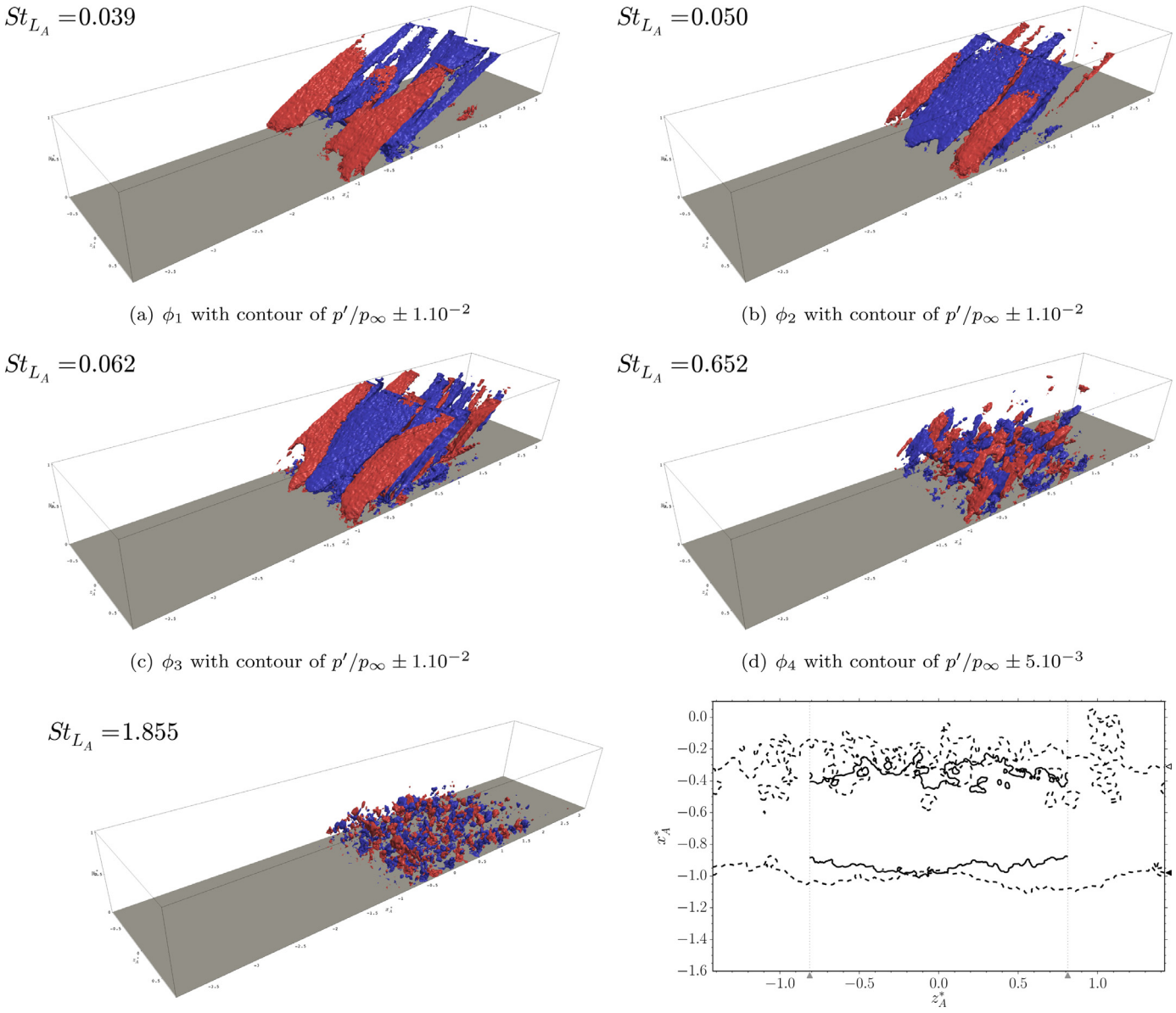

(a) ϕ_1 with contour of $p'/p_\infty \pm 1.10^{-2}$

(b) ϕ_2 with contour of $p'/p_\infty \pm 1.10^{-2}$

(c) ϕ_3 with contour of $p'/p_\infty \pm 1.10^{-2}$

(d) ϕ_4 with contour of $p'/p_\infty \pm 5.10^{-3}$

(e) ϕ_5 with contour of $p'/p_\infty \pm 5.10^{-3}$

(f) Separated area boundaries of mode ϕ_2 for two span lengths

Fig. 11. (a–e) Real part of selected DMD modes showing contours of modal pressure fluctuations. (f) Recirculation bubble boundaries of mode ϕ_2 for two different span lengths, reference case A with $L_z = 6\delta_0$ (—) and extended span with $L_z = 10.5\delta_0$ (- - -). (▲) indicate the spanwise limits of case A with $L_z = 6\delta_0$. (◀) and (◁) denote the separation and reattachment lines, respectively.

medium frequency mode seem to grow along the dividing streamline and are convected downstream of the interaction region, where they impact the reattachment compression waves downstream of the SBLI. This is consistent with the findings of Pasquariello et al. (2017).

Finally, the high-frequency mode ϕ_5 at $St_{L_A} = 1.855$ in Fig. 11(e) exhibits pressure field modulations, originating from the reflected shock foot and separation line, that are convected along the mean sonic line, downstream of the interaction (see animation available online). The modal shapes highlight a growth of these perturbations in the first half of the SBLI and their frequency is related to the large scale structures evolving in the TBL.

These results support that the broadband low-frequency unsteadiness of the reflected shock foot undergoes a complex motion dynamics with a streamwise back and forth mechanism modulated by spanwise oscillations. Furthermore, low-frequencies are dominant at the reflected shock foot location whereas the TBL high-frequencies related structures appear to be amplified by the shock system.

3.2. Micro vortex generators

In the following section, we focus on the controlled SBLI by means of microramps. To clarify the wake-flow features of these microramps and the modifications to the TBL before the interaction with the shock wave, we first characterize the flow field organization around and downstream of the mVGs. To gain insight into the mechanisms induced on the mean flow, the time-averaged velocity field distribution is measured at $y = 0.5h$ above the wall. The mean velocity is reported in the form of $(\langle U_B \rangle - \langle U_A \rangle)/U_e$, where $\langle U_{A,\,B} \rangle$ denotes the time-averaged velocity field of case A or B and U_e the velocity at the edge of the TBL. Fig. 12 shows the velocity differences for three different streamwise locations downstream of the mVGs obtained in the present LES, and compared with Wang et al. (2012) measurements. An overall good

agreement is obtained with the experimental data and a velocity deficit behind each mVG is retrieved. This velocity defect is rapidly cancelled, even if the mean longitudinal velocity in case B remains slightly below the one measured in the uncontrolled case A far downstream of the mVGs. On the contrary, two high speed regions are found on each side of the median plane of the mVGs. These maxima of velocity excesses remain approximately constant around 0.07 downstream of the mVGs. It should be noted that between the mVGs ($z = 0$), an increased velocity appears in the near field behind the mVGs rake in case B, which rapidly recovers to case A mean velocity further downstream.

To characterize more precisely the momentum added by the control devices to the TBL near wall region, we tracked the development of the added momentum flux downstream of the mVGs, using the metric introduced by Giepman et al. (2014) in its compressible form:

$$E(x) = \int_0^h \frac{\langle\rho_B\rangle\langle U_B\rangle^2 - \langle\rho_A\rangle\langle U_A\rangle^2}{\rho_\infty U_\infty^2} \mathrm{d}y \tag{3}$$

The selected upper integration bound is $y = h$ since the separation bubble has been found to be mostly sensitive to the momentum flux contained in the region $y = [0, 0.43\delta_0]$. Furthermore, according to Giepman et al. (2014)and van Oudheusden et al. (2011), the development of the added momentum flux $E(x)$ is relatively independent of the chosen upper integration bound.

Fig. 13 shows the development of the normalized added momentum flux $E(x)/h$ for different spanwise locations. These locations are described in Fig. 2: z_{50}, z_{25} and z_0 are located on the mVG, whereas $z = 0$ is located between the two mVGs. Four regions can be distinguished downstream the mVGs: a mixing region, a plateau, a shock zone and post-shock region. These regions appear regardless of the spanwise location but with different trends and strengths. During the initial mixing phase, a momentum deficit is observed downstream of the mVG, at z_0, where low-momentum fluid taken from the near wall region is transported towards higher altitude of the TBL by the two counter-rotating streamwise vortices arising from each side of the mVGs, *i.e.* on both sides of the z_0 plane. The momentum deficit decreases with the downstream distance as a consequence of the wake moving away from the surface due to an upwash mechanism. However, for the z_{25} spanwise station, the aforementioned streamwise vortices then transport high-momentum fluid from the outer TBL towards the surface, leading to the momentum excess observed in the mixing region at this spanwise location. The z_{50} and $z = 0$ locations only present a slight momentum excess which is rapidly cancelled further downstream. The mVG wake area of influence is therefore located between the z_0 and z_{50} locations as observed in Fig. 12.

The mixing region is followed by a plateau, which extends over approximately L_{sep_B} until the reflected shock foot is encountered. For all spanwise stations, the added momentum flux $E(x)$ remains almost constant with a momentum criterion equal to $E(x)/h = -0.08$ for z_0, 0.15 for z_{25} and 0.01 for z_{50} and $z = 0$ locations. This plateau region may indicates that the mVGs could be located closer to the interaction region without reducing their efficiency. Regarding the shock region, the added momentum is amplified when crossing the reflected shock wave for all spanwise locations. A peak of added momentum is observed at the same streamwise location $x_B^* = -1$, followed by a rapid relaxation of $E(x)$ to zero, except for z_{25}. Finally the post-shock region shows an increase of momentum flux downstream the interaction for all spanwise locations apart from z_0 where after a slight increase of $E(x)$ in the vicinity of the incident shock wave, a significant increasing momentum deficit can be observed.

Figs. 12 and 13 highlight the influence of the mVGs on the mean flow. However, we have shown in our previous study, Grébert et al. (2016), that large-scale vortices are periodically shed downstream of the mVGs. In order to investigate the mVGs' wake unsteady dynamics, we placed numerical probes downstream of the mVGs with the same data acquisition parameters as used for the wall-pressure fluctuations in Section 3.1. The total integration time for the controlled case B allow to capture 32 low-frequency oscillations. The probes used to get deeper insight into the mVG's wake dynamics are located at 4 different altitudes $y = [0.5, 0.75, 1.0, 1.25]\delta_0$ and cover a streamwise distance of $x_B^* = [-3.7, 2.6]$ around and downstream of the mVGs. We focus in the following on the probes located along the centre location z_0 of each mVG and along the median plane between them ($z = 0$). For the sake of brevity, we only present the pressure fluctuations at the highest altitude $y = 1.25\delta_0$. This altitude corresponds to the edge of the TBL, where the large-scale vortices are expected to be the only existing highly coherent structures. All conclusions drawn hereafter also apply with the other flow data recorded on the same array of probes.

Fig. 14 shows the pressure fluctuations spectra downstream of the mVGs and in the interaction region. The spectra are obtained using Welch's algorithm with signals split in 6 segments with 50% overlap and Hann windows. In order to emphasize the frequencies that contribute the most, we present the weighted PSD, normalized by the integrated PSD over all frequencies, *i.e.*, $f \cdot PSD(f)/\int PSD(f)\mathrm{d}f$. Fig. 14(b) shows the spectrum in the centre location of the mVGs, z_0. A ridge can be clearly seen on the contour map centred on a constant frequency of $St_{L_A} = 2.4$. This ridge remains after passing the interaction system but then decays rapidly downstream. This particular frequency of $St_{L_A} = 2.4$

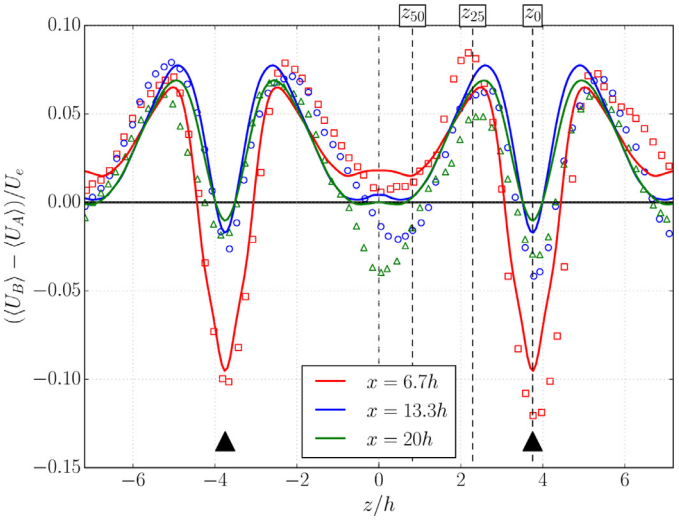

Fig. 12. Time-averaged velocity differences downstream of the mVG at $y = 0.5h$. Symbols represent (Wang et al., 2012) measurements. Black triangles indicate the spanwise locations of the mVG (size of mVGs not to scale).

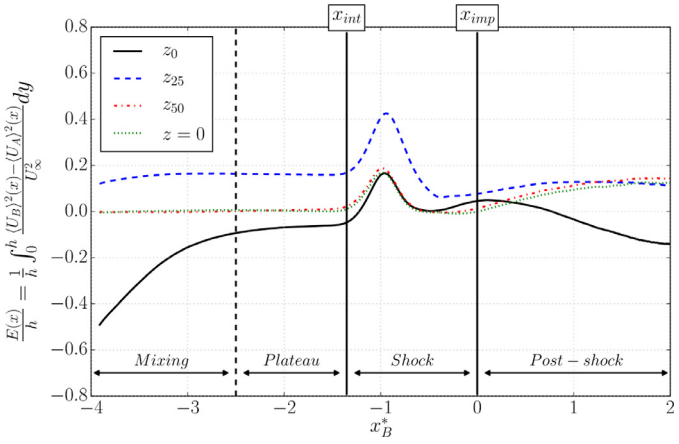

Fig. 13. Streamwise development of the normalized added momentum flux E/h downstream of the mVGs for 4 different spanwise locations.

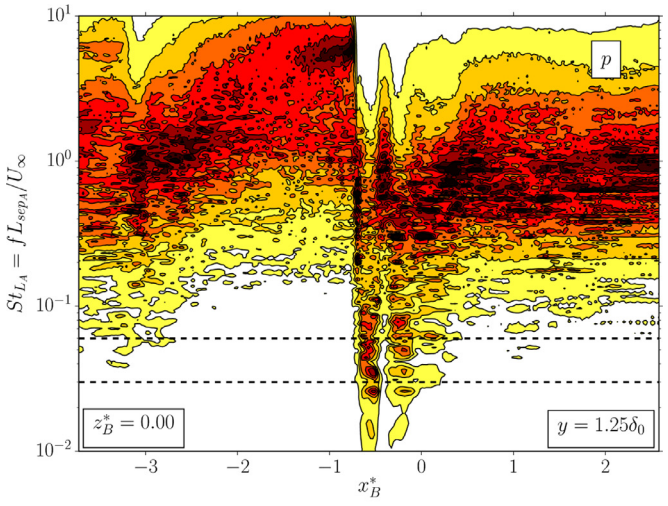

(a) Between the mVGs (case B).

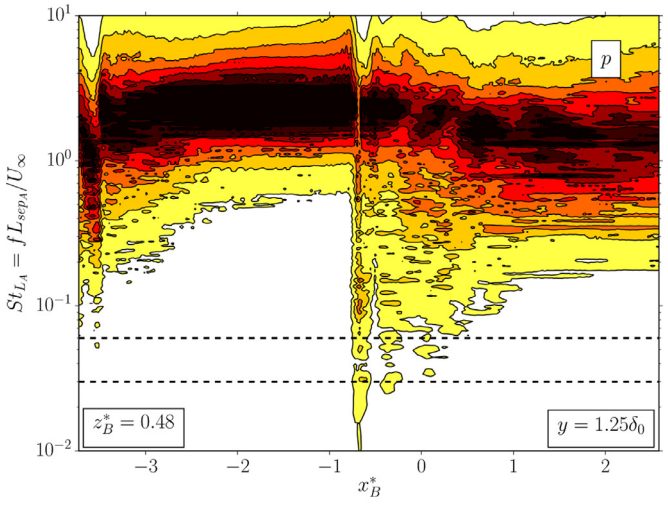

(b) Center location z_0 of the mVGs (case B).

Fig. 14. Weighted PSD spectra of pressure fluctuations at $y = 1.25\delta_0$ (case B). Contour: $f \cdot PSD(f)/\int PSD(f)df$ (same arbitrary scale).

corresponds to the large scale vortices shed in the wake of the mVGs. Indeed, Fig. 14(a), shows the spectrum between the mVGs, $z = 0$, and no ridge can be found around this particular frequency. A non-negligible energy content can instead be found in the high frequency range $St_{L_A} \geq 1$ corresponding to the characteristic frequency of the energetic scales in the undisturbed TBL. This energy content shifts to lower frequencies downstream the SBLI as a result of the thickening of the TBL past the shock system. Finally the same low-frequency broadband activity as observed in Fig. 8 can be seen in the region near the reflected shock foot in Fig. 14(a) but vanishes under the influence of the mVGs in Fig. 14(b). The SBLI between the mVGs appears to remain unaffected by the unsteady dynamic arising from large-scale vortices periodically shedding downstream of the mVGs at $St_{L_A} = 2.4$. This spatio-temporal dynamics tend to induce a local unsteady forcing onto the interaction region affected by the wake of the mVGs, modulating the low-frequency motion of the reflected shock foot. We will thus focus on the SBLI region in the following section in order to investigate this point.

3.3. Controlled SBLI

In this section, we provide a cross-comparison between the controlled case B and the baseline case A, regarding the SBLI. In order to investigate the frequency content of the interaction region, weighted PSD of wall-pressure fluctuations are presented in Fig. 15. The spectrum, for case B is obtained following the same procedure as the one used for Fig. 14. It should be noted that in case A, the spectrum is computed using averaged wall-pressure signals in the spanwise (homogeneous) direction, whereas in case B the spectra are averaged using the spatial symmetries of the computational domain, *i.e.* using four symmetric spanwise locations only.

A first remark is that no forcing is found on all spectra for case B, in the upstream TBL in the medium and low frequency ranges as was highlighted in Section 3.1. For case A, Fig. 15(a), all characteristics have already been identified in previous Section 3.1 and the low-frequency dynamics exhibits a peak at $St_{L_A} = 0.038$ and $St_{L_A} = 0.05$. The same low-frequency motion can be seen in case B but with different characteristic frequencies depending on the spanwise location. Between the mVGs, Fig. 15(b) at a spanwise location of $z_B^* = 0$, the low-frequency content is characterized by the same frequencies with peaks at $St_{L_A} = 0.038$ and $St_{L_A} = 0.05$. In the wake of the mVGs, Fig. 15(c) at $z_B^* = 0.48$ (or z_0), the low-frequency activity has been reduced in terms of intensity and shifted to higher frequencies with a peak at $St_{L_A} = 0.1$, twice the frequency observed at $z_B^* = 0$.

Furthermore, the PSD levels (in arbitrary units) for the low-frequency range, $St_{L_A} = 0.033 - 0.038$, increase in between the mVGs as compared to the reference case A, with values of 0.18 and 0.125 respectively. On the contrary, we measure a PSD level of 0.08 in the direct wake of the mVGs. This indicates that the reflected shock foot low-frequency dynamics is locally intensified between the mVGs, but that the overall intensity of this phenomenon has decreased if we consider the entire span of the domain.

Thus, the wall-pressure spectra of the controlled case B display modifications of the low-frequency motion of the reflected shock foot. The characteristic frequency of $St_{L_A} = 0.05$ in the uncontrolled case A has been altered and shifted to a higher $St_{L_A} = 0.1$ frequency in the wake of the mVGs, while it remains the same at $z_B^* = 0$ between the mVGs. This means that the local interaction of the mVG's wake with the SBLI system seems to break the spanwise direction homogeneity of the uncontrolled case, leading to selected low-frequency motion of the reflected shock foot according to the new spanwise period.

Another point of interest for the controlled SBLI is the size of the separation bubble. Fig. 16, shows the time-averaged skin-friction lines in both cases considered in this paper. In case A, Fig. 16 (top), it seems that we retrieve the results found by Pasquariello et al. (2017) regarding the formation of streamwise Görtler-like vortices downstream of the SBLI. These vortices manifest their presence through their imprints on the skin friction lines close to the reattachment region, where converging/diverging lines corresponding to vortex-induced upwash and downwash can be observed along the reattachment location, indicating a spanwise modulation of the flow in this region. It should be noted that these traces, corresponding to the streamwise Görtler-like vortices, are attenuated in our case compared to Pasquariello et al. (2017) results. This can be explained by the fact that the intensity of the present SBLI is much lower than in Pasquariello et al. (2017), so that the size of the separation region and the associated curvature of the streamlines is less pronounced than in their study. Consequently, these Görtler-like vortices are more difficult to highlight, especially with the long averaging time of 50 low-frequency oscillations taken into account in our case A. Moreover, it cannot be excluded at this stage that longitudinal streaks could also play a role in the observed spanwise modulation of the flow close to the reattachment line. For the controlled SBLI, a clear shift to further downstream location of the convergence line corresponding to separation can be observed, as well as an undulation of this line which was nearly straight in the spanwise direction in the uncontrolled case. The divergence line corresponding to reattachment also displays a wavy pattern, but its mean location remains pretty much the same as in case A. In case B, node and saddle points can clearly be identified along the

separation and reattachment lines, which was not so clear in the uncontrolled case. Moreover, the streamwise size of the recirculation bubble strongly varies in the spanwise direction in case B, with a minimum located in the high speed zones and added momentum flux regions identified in Figs. 12 and 13, respectively. Furthermore, a new organization of the recirculation bubble appears in the controlled case, with saddle and focus points on each side of the mVGs centreline. Such patterns of the skin-friction lines are related to tornado-like vortices escaping from the separation bubble. Finally, by computing the area between the main convergence and divergence lines in both cases, we observe a 20% decrease of the separation area in case B compared to case A.

Regarding the reflected shock foot motion and in order to characterize its distance of excursion, we use the intermittency factor $\gamma_i(x, z)$ as introduced by Dolling and Or (1985) and defined as:

$$\gamma_i = \frac{\int_{t_1}^{t_2} \begin{cases} 1, & p_w > \langle p_{w,0} \rangle + 3\sigma_{p_{w,0}} \\ 0, & \text{else} \end{cases} \mathrm{d}t}{t_2 - t_1} \tag{4}$$

with $\langle p_{w,\,0} \rangle$ and $\sigma_{p_{w,0}}$ being the time-averaged wall-pressure and associated standard deviation measured at $x_A^* = -2.5$ in the upstream TBL. This intermittency factor $\gamma_i(x, z)$ represents the fraction of time during which the wall-pressure p_w is above a threshold value defined by the upstream TBL. Based on this factor, it is possible to derive an intermittent length scale $L_i(z)$ corresponding to the region where, for each spanwise station z, we have: $0.01 < \gamma_i(x,\ z) < 0.99$. For the uncontrolled case, we report a spanwise-averaged intermittency length scale $\langle L_i \rangle_z = 1.15\delta_0$, and a high intermittency level equal to $\langle \gamma_i(x_s) \rangle_z = 0.87$ at the mean separation point (see Fig. 17). These results compare well with the literature: Pasquariello et al. (2017) reported a value of $\gamma_i(x_s) = 0.84$ and $L_i = 1.2\delta_0$, and Loginov et al. (2006) found $\gamma_i(x_s) = 0.88$ and $L_i = 1.3\delta_0$.

In Fig. 18, we report the spanwise evolution of the intermittent length scale for the uncontrolled and controlled cases. Only part of the domain is reported, refer to Fig. 12 for the spanwise locations z_0, z_{25} and z_{50}. In case A, $L_i(z)$ remains approximately constant throughout the complete span. However, case B exhibits strong modulations of $L_i(z)$ as shown in Fig. 16. Its value is below the uncontrolled case for $z_B^* = [z_0, z_{25}]$, with a 16% decrease at z_0. This area is located between the two streamwise vortices originating from the sides of the mVGs. For the spanwise locations between z_{25} and z_{50}, $L_i(z)$ is noticeably increased, with a peak of $L_i = 1.56\delta_0$ at $z_B^* = 0.22$. This location corresponds to the outward edge of the aforementioned vortices. Between the mVGs at $z_B^* = 0$, the intermittent length scale remains above case A with a value of $L_i = 1.3\delta_0$. It should be noted that, in case B, the intermittency boundary of $\gamma_i = 0.99$ remains almost homogeneous in the spanwise direction, whereas the $\gamma = 0.01$ boundary is highly modulated in this direction, see Fig. 16. Furthermore, under the control of the mVGs, the area of excursion of the shock wave is increased by 15% compared to case A.

At last, we focus on the fluctuating pressure loads which are one of the most detrimental effect for the structures affected by a SBLI system. We introduce the following metric in order to characterize the influence of the mVGs on the loads sustained by the wall:

$$I_{F_{\bar{S}}'}(x) = \frac{\sqrt{\langle F_{\bar{S}}'^2 \rangle}(x)}{\langle F_{\bar{S}} \rangle(x)} \quad \text{with} \quad F_{\bar{S}}(x, t) = \int_z p_w(x, z, t)\, ds \tag{5}$$

Using this metric $I_{F_{\bar{S}}'}(x)$, we retrieve the partial pressure loads on the wall surface using the pressure probes data. Pressure loads are only partial due to the incomplete discretization of the pressure probes in the spanwise and streamwise directions.

Fig. 19 shows the streamwise evolution of $I_{F_{\bar{S}}'}(x)$ in the interaction region for cases A and B. One can observe a clear shift of the streamwise location of the maximum of $I_{F_{\bar{S}}'}(x)$ for the SBLI under the control of

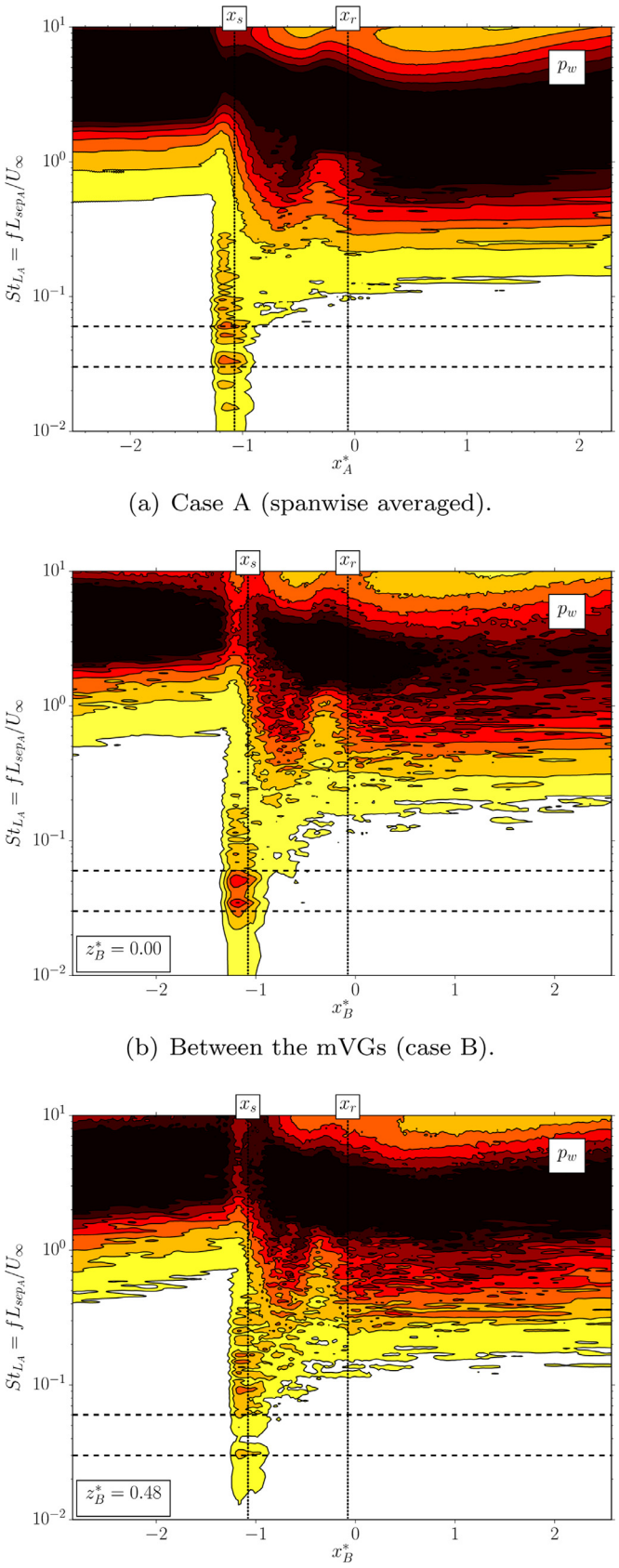

Fig. 15. Weighted PSD spectra of wall-pressure fluctuations. Horizontal dashed lines indicates $St_{L_A} = 0.03$ and $St_{L_A} = 0.06$. Contour: $f \cdot PSD(f)/\int PSD(f)df$ (same arbitrary scale). Black vertical lines indicates the mean edges of the separation bubble.

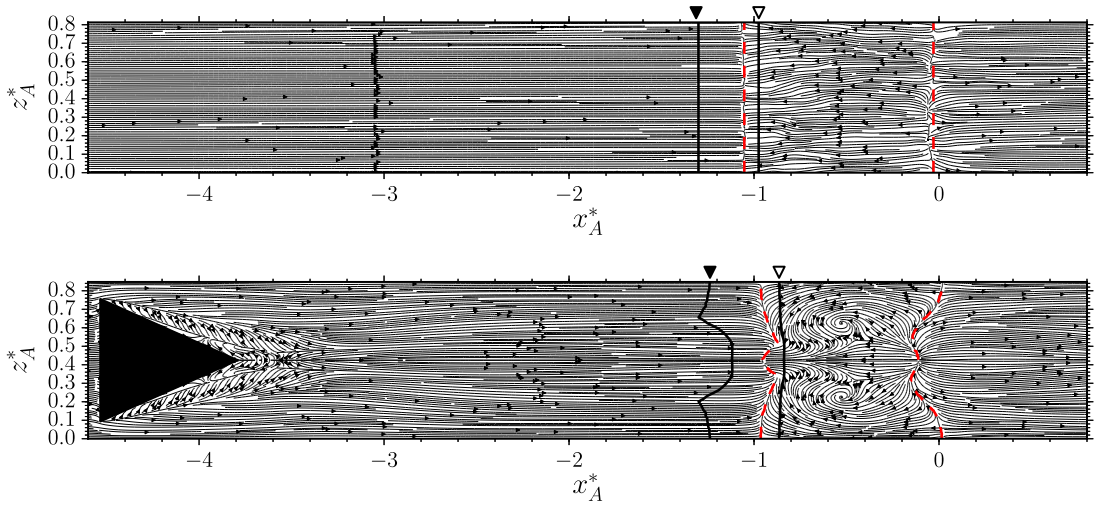

Fig. 16. Time-averaged skin friction lines for: case A without control (top) and case B with control (bottom). Only half of the computational domain is reported. Black solid lines (—) indicate the intermittency boundaries $\gamma_i = 0.01$ (▽) and $\gamma_i = 0.99$ (▼). Dashed red lines (- - -) show the separation and reattachment locations. (For interpretation of the references to colour in this figure legend, the reader is referred to the web version of this article.)

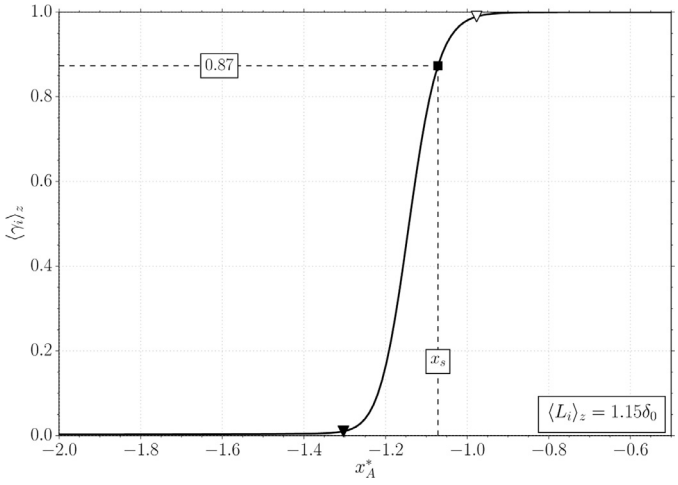

Fig. 17. Intermittency factor $\langle \gamma_i(x) \rangle_z$ for the uncontrolled case A. Intermittency boundaries $\langle \gamma_i \rangle_z = 0.01$ and $\langle \gamma_i \rangle_z = 0.99$ are indicated by (▼) and (▽), respectively..

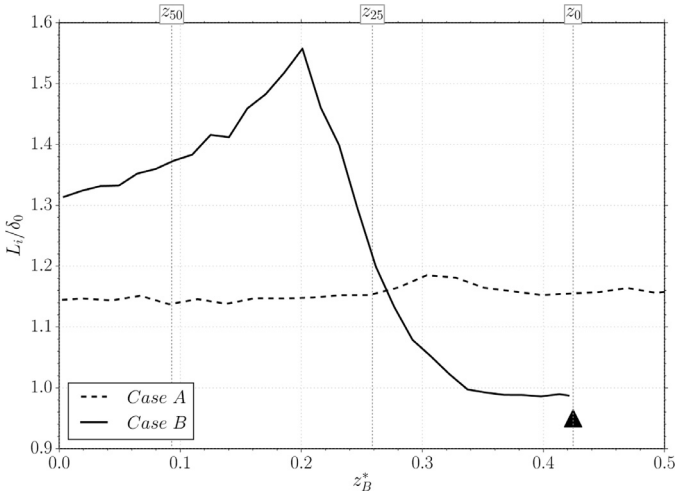

Fig. 18. Spanwise evolution of the intermittent length scale for case A (- - -) and case B (—). The black triangle indicates the spanwise location of the mVG (size not to scale). Refer to text and Fig. 12 for the z_0, z_{25} and z_{50} locations.

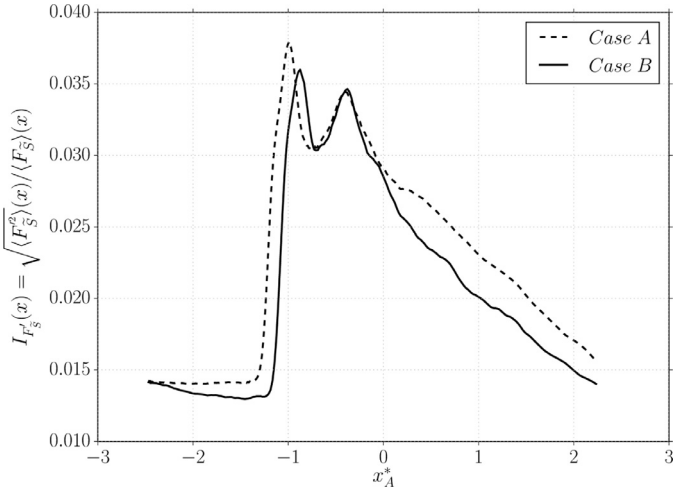

Fig. 19. Streamwise evolution of pressure loads intensity of case A (- - -) and case B (—).

mVGs. This is consistent with the observations made on Fig. 16 and confirms the further downstream location of the separation point in case B. Moreover, the amplitude of this peak is lowered. Regarding the second peak, their levels and streamwise locations remain identical between the two cases, confirming that the reattachment point in almost unaffected by the mVGs. Finally, downstream of the interaction region, pressure relaxation is enhanced yielding to lower pressure loads in case B. Therefore, by integrating $I_{F_{\tilde{S}}'}(x)$, pressure loads in the controlled case B exhibit a 9% decrease compared to the reference case A.

4. Conclusion

We conducted in this work two wall-resolved, long-time integrated large-eddy simulations of the SBLI configuration, with and without the control of upstream microramp vortex generators. These simulations were based on the experimental configuration of Wang et al. (2012), where a wedge-induced shock wave is generated by a flow deflection angle of $\phi = 10.5°$ and impacts a TBL developing at a Mach number of $M = 2.7$ and a Reynolds number of $Re_\theta = 3600$ at x_{imp}. Validation of the numerical approach and SBLI characterization of the natural case have been successfully performed with unsteady analyses. Pressure

fluctuations spectra showed that the shock system undergoes a complex dynamics involving broadband low-frequencies related to the reflected shock foot motion. Three-dimensional dynamic mode decomposition was also conducted to complement the analysis and proved to be efficient in identifying the different modes of the SBLI unsteadiness. Interestingly, the low-frequency motion of the reflected shock wave has been found to be composed of different modes of streamwise back and forth movement together with spanwise undulations.

Two microramp vortex generators have then been introduced in the computational domain upstream of the interaction system. Study of the flow downstream of the microramps showed good agreement with the reference experiments. The momentum deficit in the wake of the mVGs and the two surrounding high speed regions on each side of the wake were correctly reproduced. The momentum flux added to the near wall region, $E(x)$, exhibits four different regions downstream of the mVGs, among which a plateau can be observed immediately upstream of the SBLI, with $E(x)$ approximately constant and only little momentum added to the near wall region. This plateau tends to indicate that the mVGs could be placed closer to the interaction without reducing their efficiency. In our configuration, the microramps appear to be more effective at off-centre locations z_{25} (within the high speed regions) with a separation length reduced by nearly 30% compared to the uncontrolled case. A new organization of the recirculation bubble has also been observed in the controlled case with tornado-like vortices emerging at z_{25} in the separated area. In the centre location of the mVGs z_0, a momentum deficit is observed all the way downstream of the mVGs up to the interaction region, and the length of the separation bubble is only reduced by 15%. These findings are at odds with Giepman et al. (2014) who investigated identical microramps at different flow conditions, $M = 2$ and $Re_{\theta_i} = 2.18 \times 10^4$. In the present work, the separated area has been reduced by 20% compared to the clean configuration. Furthermore, the mVGs wake exhibited a shedding of periodic coherent structures at a characteristic frequency of $St_{L_A} = 2.4$.

Regarding the unsteadiness of the reflected shock foot, the mVGs triggered a new undulating motion with different characteristic low-frequencies in the spanwise direction: $St_{L_A} = 0.05$ between the mVGs and reduced motion at $St_{L_A} = 0.1$ in the centre location of the mVGs. These frequencies differ from the uncontrolled case where a low-frequency motion at $St_{L_A} = 0.06$ has been found. The distance of the excursion of the reflected shock foot is also affected by the mVGs with strong modulation in the spanwise direction. Its value is reduced by 16% in the centreline of the mVGs where $L_i = 1.0\delta_0$, whereas a peak of $L_i = 1.56\delta_0$ is observed at the outward edges of the mVGs' wake. Furthermore, we showed that the intermittency boundary of $\gamma_i = 0.01$ is the most affected in the spanwise direction by the wake of the mVGs, whereas the $\gamma_i = 0.99$ boundary remains nearly spanwise-homogeneous. The total area of excursion of the reflected shock foot, in case B, has been increased by 15% compared to the uncontrolled case. Finally, in the controlled case, the pressure loads have been reduced by 9% in the interaction region. Moreover, the fluctuating pressure loads display a lower maximum level in the vicinity of the reflected shock foot and lower levels downstream of the interaction when the mVGs are present.

Acknowledgements

This research was supported in part by the French Ministry of Defense through financial support of the DGA and the region of Occitanie – Pyrénées Méditerranée. Authors would like to thank the continuous support and computational resources provided by CNRS on `Turing`, `Occigen` (GENCI-IDRIS grant x2016a7178 and GENCI-CINES grant A0022A07178), `Eos` (CALMIP, grants 2016-p1425 and 2017-p1425). We also acknowledge PRACE for awarding us access to `JUQUEEN` at JSC/Forschungszentrum Juelich, Germany (GSC/JSC grant 2016153674).

Supplementary material

Supplementary material associated with this article can be found, in the online version, at 10.1016/j.ijheatfluidflow.2018.05.001.

References

Anderson, B.H., Tinapple, J., Surber, L., 2006. Optimal control of shock wave turbulent boundary layer interactions using micro-array actuation. AIAA Paper 3197 (June), 1–14.

Aubard, G., Gloerfelt, X., Robinet, J.-C., 2013. Large-Eddy simulation of broadband unsteadiness in a shock/boundary-layer interaction. AIAA J. 51 (10), 2395–2409. http://dx.doi.org/10.2514/1.J052249.

Belson, B.A., Tu, J.H., Rowley, C.W., 2014. Algorithm 945. ACM Trans. Math. Software 40 (4), 1–23. http://dx.doi.org/10.1145/2616912.

Bermejo-Moreno, I., Campo, L., Larsson, J., Bodart, J., Helmer, D., Eaton, J.K., 2014. Confinement effects in shock wave/turbulent boundary layer interactions through wall-modelled large-eddy simulations. J. Fluid Mech. 758, 5–62. http://dx.doi.org/10.1017/jfm.2014.505.

Clemens, N.T., Narayanaswamy, V., 2014. Low-Frequency unsteadiness of shock wave/turbulent boundary layer interactions. Annu. Rev. Fluid Mech. 46 (September), 469–492. http://dx.doi.org/10.1146/annurev-fluid-010313-141346.

Dolling, D.S., Or, C.T., 1985. Unsteadiness of the shock wave structure in attached and separated compression ramp flows. Exp. Fluids 3 (1), 24–32. http://dx.doi.org/10.1007/BF00285267.

van Driest, E.R., 1951. Turbulent boundary layer in compressible fluids. J. Aeronaut. Sci. 18 (3), 145–160. http://dx.doi.org/10.2514/8.1895.

Dupont, P., Haddad, C., Debiève, J.-F., 2006. Space and time organization in a shock-induced separated boundary layer. J. Fluid Mech. 559, 255. http://dx.doi.org/10.1017/S0022112006000267.

Eitel-Amor, G., Örlü, R., Schlatter, P., 2014. Simulation and validation of a spatially evolving turbulent boundary layer up to Re_θ 8300. Int. J. Heat Fluid Flow 47, 57–69. http://dx.doi.org/10.1016/j.ijheatfluidflow.2014.02.006.

Ganapathisubramani, B., Clemens, N.T., Dolling, D.S., 2009. Low-frequency dynamics of shock-induced separation in a compression ramp interaction. J. Fluid Mech. 636, 397–425. http://dx.doi.org/10.1017/S0022112009007952.

Giepman, R.H.M., Schrijer, F.F.J., van Oudheusden, B.W., 2014. Flow control of an oblique shock wave reflection with micro-ramp vortex generators: effects of location and size. Phys. Fluids 26 (6), 066101. http://dx.doi.org/10.1063/1.4881941.

Grébert, A., Bodart, J., Jamme, S., Joly, L., 2016. Toward the characterization of micro vortex generators effects on shock wave/turbulent boundary layer interaction using LES. 11th International ERCOFTAC Symposium on Engineering Turbulence Modelling and Measurements.

Grébert, A., Bodart, J., Jamme, S., Joly, L., 2017. Simulations of shock wave/turbulent boundary layer interaction with upstream micro vortex generators. 10th International Symposium on Turbulence and Shear Flow Phenomena.

Grilli, M., Schmid, P.J., Hickel, S., Adams, N.A., 2012. Analysis of unsteady behaviour in shockwave turbulent boundary layer interaction. J. Fluid Mech. 700, 16–28. http://dx.doi.org/10.1017/jfm.2012.37.

Hildebrand, N., Dwivedi, A., Nichols, J.W., Jovanović, M.R., Candler, G.V., 2018. Simulation and stability analysis of oblique shock-wave/boundary-layer interactions at mach 5.92. Phys. Rev. Fluids 3 (1), 013906. http://dx.doi.org/10.1103/PhysRevFluids.3.013906.

Jovanović, M.R., Schmid, P.J., Nichols, J.W., 2014. Sparsity-promoting dynamic mode decomposition. Phys. Fluids 26 (2). http://dx.doi.org/10.1063/1.4863670.

Konno, K., Ohmachi, T., 1998. Ground-motion characteristics estimated from spectral ratio between horizontal and vertical components of microtremor. Bull. Seismol. Soc. Am. 88 (1), 228–241.

Lin, J.C., 2002. Review of research on low-profile vortex generators to control boundary-layer separation. Prog. Aerosp. Sci. 38 (4–5), 389–420. http://dx.doi.org/10.1016/S0376-0421(02)00010-6.

Loginov, M.S., Adams, N.A., Zheltovodov, A.A., 2006. Large-eddy simulation of shock-wave/turbulent-boundary-layer interaction. J. Fluid Mech. 565, 135–169. http://dx.doi.org/10.1017/S0022112006000930.

van Oudheusden, B.W., Jöbsis, A.J.P., Scarano, F., Souverein, L.J., 2011. Investigation of the unsteadiness of a shock-reflection interaction with time-resolved particle image velocimetry. Shock Waves 21 (5), 397–409. http://dx.doi.org/10.1007/s00193-011-0304-4.

Panaras, A.G., Lu, F.K., 2015. Micro-vortex generators for shock wave/boundary layer interactions. Prog. Aerosp. Sci. 74, 16–47. http://dx.doi.org/10.1016/j.paerosci.2014.12.006.

Pasquariello, V., Hickel, S., Adams, N.A., 2017. Unsteady effects of strong shock-wave/boundary-layer interaction at high Reynolds number. J. Fluid Mech. 823 (July), 617–657. http://dx.doi.org/10.1017/jfm.2017.308.

Piponniau, S., Dussauge, J.P., Debiève, J.-F., Dupont, P., 2009. A simple model for low-frequency unsteadiness in shock-induced separation. J. Fluid Mech. 629, 87. http://dx.doi.org/10.1017/S0022112009006417.

Pirozzoli, S., Bernardini, M., 2013. Probing high-Reynolds-number effects in numerical boundary layers. Phys. Fluids 25 (2). http://dx.doi.org/10.1063/1.4792164.

Priebe, S., Martín, M.P., 2012. Low-frequency unsteadiness in shock waveturbulent boundary layer interaction. J. Fluid Mech. 699, 1–49. http://dx.doi.org/10.1017/jfm.2011.560.

Priebe, S., Tu, J.H., Rowley, C.W., Martín, M.P., 2016. Low-frequency dynamics in a shock-induced separated flow. J. Fluid Mech. 807, 441–477. http://dx.doi.org/10.

1017/jfm.2016.557.
Schlatter, P., Örlü, R., 2010. Assessment of direct numerical simulation data of turbulent boundary layers. J. Fluid Mech. 659, 116–126. http://dx.doi.org/10.1017/S0022112010003113.
Schmid, P.J., 2010. Dynamic mode decomposition of numerical and experimental data. J. Fluid Mech. 656 (4), 5–28. http://dx.doi.org/10.1017/S0022112010001217.
Touber, E., Sandham, N.D., 2009. Large-eddy simulation of low-frequency unsteadiness in a turbulent shock-induced separation bubble. Theor. Comput. Fluid Dyn. 23 (2), 79–107. http://dx.doi.org/10.1007/s00162-009-0103-z.
Tu, J.H., Rowley, C.W., Luchtenburg, D.M., Brunton, S.L., Kutz, J.N., 2013. On dynamic mode decomposition: theory and applications. J. Comput. Dyn. (September), 1–30. http://dx.doi.org/10.3934/jcd.2014.1.391.
Vreman, A.W., 2004. An eddy-viscosity subgrid-scale model for turbulent shear flow: algebraic theory and applications. Phys. Fluids 16 (10), 3670–3681. http://dx.doi.org/10.1063/1.1785131.
Wang, B., Liu, W., Zhao, Y., Fan, X., Wang, C., 2012. Experimental investigation of the micro-ramp based shock wave and turbulent boundary layer interaction control. Phys. Fluids 24 (5), 055110. http://dx.doi.org/10.1063/1.4719146.
Xie, Z.-T., Castro, I.P., 2008. Efficient generation of inflow conditions for large eddy simulation of street-scale flows. Flow Turbul. Combust. 81 (3), 449–470. http://dx.doi.org/10.1007/s10494-008-9151-5.